Increased Spatial Randomness and Disorder of Nucleates in Dark-Phase Electrodeposition Lead to Increased Spatial Order and Pattern Fidelity in Phototropically Grown Se-Te Electrodeposits

Ethan Simonoff[†], Lorenzo X. Van Muñoz[†], Nathan S. Lewis[†,ǁ,*]

[†]Division of Chemistry and Chemical Engineering. 127-72, 210 Noyes Laboratory
[ǁ]Beckman Institute
California Institute of Technology
Pasadena, CA 91125

*Corresponding Author: nslewis@caltech.edu

TABLE OF CONTENTS (TOC) GRAPHIC.

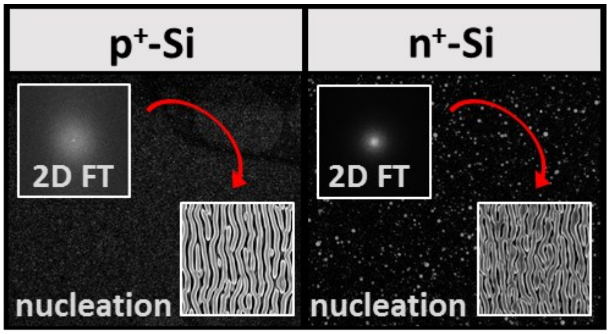

Using Se-Te as a model system, we demonstrate a fundamental light-matter interaction and show that increased spatial disorder of dark-phase nucleates intrinsically produces increased long-range order of photoelectrochemically deposited nanostructures.

ABSTRACT.

The role of nucleation was investigated during phototropic growth of Se-Te. Under low levels of mass deposition (mass equivalent of -3.75 mC cm^{-2} of charge passed) that produced small nucleate spacings, patterns in photoelectrochemically deposited Se-Te films converged at relatively earlier levels of mass deposition, and ultimately exhibited higher pattern fidelity throughout pattern development, as compared to pattern formation from larger initial nucleate spacings. Consistently, use of an applied striking potential during very early levels of mass deposition produced more spatially random dark-phase electrodeposited nucleates and led to phototropic Se-Te photoelectrodeposited films that exhibited improved pattern fidelity relative to depositions performed with no striking step. Collectively, the data indicate that increases in randomness and spatial disorder of the dispersion of the initial nucleates produces increases in the fidelity and spatial order in the resulting phototropically grown electrodeposits.

Keywords: Electrodeposition, photoelectrochemistry, photodeposition, nucleation, chalcogenide, Fourier analysis

INTRODUCTION.

In conventional methods for surface patterning and 3-D morphology control, including optical lithography, holography, or direct write methods, the spatial fidelity of the resulting pattern is directly related to the spatial order and fidelity of the stimulus. For example, in optical lithography, dither of the optical beam or imprecise spatial definition in the edges of a mask deleteriously affect the fidelity of the resulting surface pattern.[1-5] Similarly, in direct write methods or scanning probe lithographic methods, vibrations of the tip introduce spatial disorder and reduce the fidelity of the resulting material or surface film.[6-8] Spatial chemical disorder due to defects or impurities also may deleteriously affect the spatial fidelity of self-assembled, optically patterned, or electrodeposited surface films.[9-13] We have recently described the phenomenon of inorganic phototropic growth, in which full 3-D control over the morphology of an electrodeposited film can be obtained by stimulating photoelectrodeposition of materials including PbSe and Se-Te alloys with an uncorrelated, unpatterned, low-intensity light beam, from an optically isotropic solution onto an optically isotropic electrode substrate.[14-18] The growth process initially involves a dark film electrodeposition phase followed by an optically stimulated photoelectrodeposition phase, in which intrinsic near-field optical scattering in the growing material shapes the internal optical field and, in an emergent property of the material, produces a dynamic feedback with the stimulating light beam that produces long-range order in the resulting electrode film structure. We show here that in inorganic phototropic growth, randomness in the initial electrodeposit is a prerequisite for – and directly leads to – high fidelity and spatial order in the resulting phototropically grown material.

RESULTS AND DISCUSSION.

A detailed experimental procedure is provided in the Supporting Information. Se-Te films were deposited potentiostatically from an aqueous solution containing 20 mM SeO_2, 10 mM TeO_2, and 1 M H_2SO_4. Samples were illuminated with vertically polarized light from a narrow-band light-emitting diode (LED) with an intensity-weighted-average wavelength of 927 nm and a power density of 53 mW cm^{-2}. Substrates were crystalline (111)-oriented Si with a miscut angle ± 0.5°, doped degenerately with either p- or n-type dopants, and the resistivities for both substrates were < 0.005 Ω-cm.

Figure 1 shows scanning-electron-microscope (SEM) images of Se-Te deposits on p^+-Si and n^+-Si substrates during the nucleation phase of phototropic growth, i.e. after a charge density of -3.75 mC cm^{-2} had been passed, corresponding to equivalent amounts of mass deposited for each sample. Images are shown for Se-Te deposited at two different applied potentials for each substrate; these applied deposition potentials correspond to representative conditions at the positive (Figure 1a and c) and negative (Figure 1b and d) extremes of the working potential range for phototropic Se-Te growth on each substrate. The insets to the panels in Figure 1 show 2D FTs of the respective SEM images. Large-area (~2000 μm^2) images of the deposits on n^+-Si are provided in Figure S1. SEM images and analysis of reproducibility in phototropic films are provided in Figure S3. Films deposited on p^+-Si (Figure 1a and b) exhibited smaller nucleate spacings than films deposited on n^+-Si (Figure 1c and d). For both substrates, the more negative applied potential resulted in smaller nucleate spacings when all other parameters were kept constant.

The 2D FT spectra for all the SEMs in Figure 1 consisted of a single, radially symmetric peak centered around the origin showing that, at this early stage of phototropic growth, the nucleates of the films were distributed isotropically. In the grayscale 2D FT spectra of the films, more white value farther from the origin corresponds to a higher frequency of nucleates in reciprocal space and thus to a larger contribution from smaller spacings in the real-space image. Wider peaks in the 2D FT spectra thus correspond to smaller nucleate spacings for the deposits. Pair-correlation function analysis (Figure S4) corroborated the 2D FT analysis and indicated more random dispersion of the nucleates on p^+-Si than of the nucleates on n^+-Si.

Figure 1e shows the relationship between the average nucleate spacing of deposits on p^+-Si and n^+-Si and the potential applied during the deposition. The nucleate spacing was defined as the inverse of the half width at half maximum (HWHM) of the isotropic peak centered around the origin in the 2D FT spectra. See Figure S5-S7 for a description of peak fitting in 2D FT spectra. In general, for each substrate, application of a more negative potential during the deposition resulted in smaller nucleate spacings. Conditions which might be hypothesized to produce larger nucleate spacings on p^+-Si, i.e. relatively more positive applied potentials, resulted in no appreciable growth after several hours of attempted deposition. Other electrodeposited chalcogenide materials have also been observed to exhibit potential-dependent nucleation behavior. For example, the nucleation density of electrodeposited CdSe increases as the deposition potential is made more negative.[19]

Figure 2 shows the stages of development for Se-Te films grown phototropically on p^+-Si and n^+-Si substrates. Such complex three-dimensional structures spontaneously form on unpatterned substrates, with incoherent, unpatterned, low-intensity illumination, from optically isotropic aqueous solutions that do not contain any chemical-directing agents such as ligands or surfactants. The deposited Se-Te material is p-type and photoactive; there is no requirement for substrate photoactivity. Phototropic growth has been demonstrated on Au, Ti, HOPG, and degenerately doped Si substrates.[17] Although electrodeposition of Se-Te in the dark yields granular films without any long-range order, electrodeposition under uniform, low-intensity polarized light results in highly ordered periodic structures with pitches determined by the intensity-weighted average wavelength of the light, and orientations determined by the direction of polarization. These phototropic lamellar nanostructures emerge from the scattering and interference of incident light at randomly distributed optical dipoles across the growth substrate. This collective response results in a feedback mechanism by which the near-field concentration of light results in preferential mass deposition at the tips of growing lamellae.[15-18] See Figure S8-S9 for discussion and schemes that elucidate the role of optical dipole scattering and nucleation on the phototropic growth mechanism.

The development of lamellae in phototropic growth is accurately predicted by a two-step, iterative model involving Monte-Carlo mass addition weighted by the optical absorption profile of a simulated Se-Te film that predicts dark nucleation will spontaneously yield order when illuminated by light with a photon energy above the optical bandgap of the Se-Te film.[15-18] An assumption of the growth model is that localized absorption leads directly to localized mass addition, suggesting that phototropic growth is a phenomenon general to semiconductors with short minority-carrier diffusion lengths that can be electrodeposited, as has been demonstrated previously with photoelectrodeposited PbSe and CdSe films.[14, 20] Notably, Se-Te photoelectrodeposits align along the direction of optical polarization regardless of the orientation with respect to the substrate, and amorphous Se-Te films comprise the deposit itself.[15-18] Hence the helical chain arrangement of Se and Te atoms is not an important factor in determining the growth order or pattern fidelity of the photoelectrodeposit. Consistently, the mechanistic understanding and modeling of the process described herein that is in full agreement with the experimental observations only includes optical constants of the materials and Maxwell's equations, with no chemical or structural bias, directing agents, or chemically preferred or lattice-matched growth directions. Thus, under these conditions, phototropic growth is a generalizable and fundamental light-matter interaction, and is not dependent on the chemical bonding or structure of the deposited material (e.g. the helical chain arrangement of Se and Te atoms).[21-22] Previous studies have demonstrated significant amounts of amorphous material in phototropic Se-Te films; Debye-Scherrer analysis of XRD spectral features revealed the presence of nanocrystalline grains with dimensions on the order of tens of nanometers.[17] Additionally, electron dispersive X-ray spectroscopy (EDS) compositional analysis indicated statistically equivalent Se:Te atomic ratios for phototropic Se-Te films deposited on p^+-Si, n^+-Si, and Au substrates (Figure S10).

The 2D FT spectra in Figure 2 show the transformation of isotropic peaks into anisotropic features in reciprocal space, as anisotropic lamellar structures emerge from the isotropically distributed nucleates. See Figure S11 for higher resolution 2D FT spectra and a detailed analysis of features observed in 2D FT spectra during phototropic Se-Te film development. Although after the first charge step (-0.75 mC cm^{-2}) the distributions of nucleates were similar for p^+-Si and n^+-Si substrates, the distributions differed after the second charge step (-3.75 mC cm^{-2}), with smaller nucleate spacings observed on p^+-Si substrates than on n^+-Si substrates. After a charge density of -22.5 mC cm^{-2} was passed, the Se-Te deposited on n^+-Si consisted of a relatively sparse distribution of fewer, but larger, discontinuous particles, whereas the Se-Te deposited on p^+-Si formed a nearly continuous thin film. As observed in the 2D FT, both films had a mostly isotropic distribution of mass at this stage of pattern formation.

After a charge density of -37.5 mC cm^{-2} was passed, early formation of lamellar structures was observed for Se-Te deposited on both p^+-Si and n^+-Si substrates. The deposited particles adopted an elliptical shape, elongated in the vertical direction, parallel to the axis of polarization. At this stage in the deposition, the elliptical particles were larger, more elongated, and more sparsely distributed on n$^+$-Si than p$^+$-Si. After charge densities of -52.5 and -67.5 mC cm^{-2} had been passed on n$^+$-Si substrates, the Se-Te deposited still appeared as vertically oriented elliptical particles with narrower spacing in the horizontal than in the vertical direction, although the number and size of the particles increased as more charge was passed. In contrast, after -52.5 mC cm^{-2} of charge density had passed on p$^+$-Si, the Se-Te appeared as vertically oriented particles made of ellipses that had begun to merge along the vertical direction. The lamellar morphology was more fully formed after 67.5 mC cm^{-2} had been passed on p$^+$-Si.

Although qualitatively similar lamellar structures ultimately formed on both p$^+$-Si and n$^+$-Si, key differences during the early stages of growth influenced the fidelity of the resulting structures. Substantial discontinuity in the Se-Te deposits was present on n$^+$-Si at charge densities for which a continuous, thin layer of nucleates was observed on p$^+$-Si. Discontinuity and larger nucleate spacings contributed to the "kinked" lamellar morphology observed on n$^+$-Si, whereas smaller nucleate spacings contributed to the straighter lamellae and higher fidelity patterns observed on p$^+$-Si. Low-magnification, wide-area SEM images of the films in Figure 2 (j) and (t) are provided in Figure S2.

Figure 3 shows the relationship between the spacing of nucleates at an early stage in the deposition (-3.75 mC cm^{-2}) and both the period (Figure 3a) and fidelity (Figure 3b) of the lamellar pattern that developed in the films after a charge density of -750 mC cm^{-2} had been passed. The figure of merit used to describe the fidelity of the pattern was the vertical full width and half maximum (FWHM) in angular units of the primary peak in the 2D FT of the pattern. See Figure

S7 and Equation S1 for a discussion of the conversion of 2D FT to radial coordinates and pattern fidelity.

The lamellar period in phototropic Se-Te films illuminated with 927 nm light is predicted by our growth model[15-18] to be 331 nm, and corresponds to $\lambda/2n$, where λ is the illumination wavelength and n is the index of refraction of the medium in which the phototropic growth occurs, equal to 1.4 (the index of refraction of the aqueous sulfuric acid solution). In Figure 3, small (≤ 50 nm) nucleate spacings were observed for depositions onto p^+-Si substrates for all applied potentials tested, whereas the nucleate spacings observed for depositions onto n^+-Si substrates were generally larger and were as high as ~225 nm. Smaller spacings between nucleates resulted in patterns with smaller periods that approached the predicted $\lambda/2n$ value. Smaller spacings between nucleates also resulted in patterns with higher fidelities. The observations of a smaller lamellar period and straighter lamellae for certain films suggest that more closely packed lamellae develop under conditions that produce closely spaced nucleates in the early stages of mass deposition.

Given the potential dependence of nucleation,[23-30] potential-striking steps are often used to increase the quality of electrodeposited films. For instance, inclusion of a strike step reduces the porosity of electrodeposited gold films.[31] Figure 4 shows SEM images and 2D FT spectra of Se-Te films that were phototropically grown on p^+-Si (Figure 4a - e) and n^+-Si (Figure 4f - j) using varied striking potentials for the first -3.75 mC cm^{-2} of mass deposition (corresponding to 0.5% of the total mass deposited). Following the initial striking step, the remaining 99.5% of mass (-746.25 mC cm^{-2}) was deposited at a relatively more positive potential (-80 mV on p^+-Si and -200 mV on n^+-Si). See Figure S12 for a graphical depiction of the striking potential experiments. As observed in Figure 1e, a wide range of nucleate spacing can be accessed for Se-Te films grown on n^+-Si substrates by tuning the deposition potential. The striking step was performed using a more negative potential than the subsequent mass-addition step, and consistently, smaller nucleate spacings were consequently produced on n^+-Si substrates than would have been produced if the entire deposition were performed at the potentials used for the mass-addition step. When performed entirely at the potentials applied during striking steps, depositions on n^+-Si do not result in purely phototropic Se-Te films. Rather, dark growth is a major contribution at later stages of mass-addition when applying these more negative potentials (Figure S13). The direct effects of nucleate spacing on the fidelity of lamellar patterns formed in Se-Te films were thus measured by varying the deposition potential during the earliest stage of mass deposition while using the same potential for deposition of the majority of the mass.

Films grown on p^+-Si with a striking step (Figure 4b - e) were similar in appearance to the control sample (Figure 4a). Films grown on n^+-Si, however, changed in appearance relative to the n^+-Si control when a striking step was added. The control sample on n^+-Si (Figure 4f) exhibited short, discontinuous lamellae and pattern defects such as dislocations and interstitial features. Relative to the control sample on n^+-Si, samples grown with a striking step (Figure 4g - j) exhibited straighter, more continuous lamellae and fewer pattern defects. This improved fidelity was also observed as sharpening of the peaks in the 2D FT as the striking potential was made more negative. As evident in both the 2D FT spectra and the SEM images, the fidelity of phototropic Se-Te films was strongly influenced by the morphology of the very earliest levels of mass addition.

Figure 5 shows the relationship between the striking potential and fidelity of phototropic Se-Te films, described by the vertical FWHM of the primary peak in the 2D FT. The trend observed in the SEM images and 2D FT spectra in Figure 4 is reflected in Figure 5, showing an improvement in the pattern fidelity of phototropic Se-Te films deposited on n^+-Si as the striking potential was made more negative. Figure 5 also shows the effects of a longer striking step at 1.0%

of total mass deposited (-7.5 mC cm^{-2}). When performing the striking step for 1.0% versus 0.5% of mass deposited, phototropic Se-Te films did not require as negative a striking potential to exhibit improved pattern fidelity, suggesting that nucleate spacing decreases with increasing amounts of deposition under these conditions. In contrast, phototropic Se-Te films on p$^+$-Si showed no improvement over the control sample when the striking step was performed for either 1.0% or 0.5% of mass deposited. Furthermore, at the conditions tested, films on n$^+$-Si reached an apparent upper limit of pattern fidelity near to what was observed on p$^+$-Si, ~30° for the vertical FWHM. The limit of pattern fidelity in Se-Te films is also reflected in the average particle-to-particle spacing data in Figure 1e, which shows nucleate spacing values for n$^+$-Si approaching values observed on p$^+$-Si as the applied deposition potential is made more negative. Both observations suggest that below a critical level of nucleate spacing, ~50 nm, no further contribution to improved pattern fidelity is obtained for the conditions tested.

The results suggest that the deposition of Se-Te on n$^+$-Si follows a progressive nucleation mechanism, rather than an instantaneous nucleation mechanism.[32] Progressive nucleation mechanisms, such as the Volmer-Weber mechanism, are characterized by 3D island growth, which has also been observed in the electrodeposition of other chalcogenide materials, such as PbTe on n-Si.[33] In an electrochemical system exhibiting instantaneous nucleation, all electrochemically active sites are nucleated during the initial stages of mass addition, and the nucleation density does not change substantially with the amount of mass deposited.[34] No substantial change was observed in the Se-Te nucleate spacings on p$^+$-Si at different applied deposition potentials nor was a change in the fidelity of phototropic Se-Te films on p$^+$-Si observed when a striking step was included, so the results are consistent with either an instantaneous nucleation mechanism or a relatively higher rate of progressive nucleation during Se-Te nucleation on p$^+$-Si. The nucleate spacings on n$^+$-Si substrates decreased as the applied potential was increased negatively, suggesting that the nucleation mechanism is potential-dependent. Thus, progressive nucleation on n^+-Si demonstrated increased nucleation rates as the applied deposition potential was made more negative, potentially approaching an instantaneous nucleation mechanism.

Although electrochemical nucleation is widely known to exhibit a substantial potential dependence due to the mass transport and diffusion of charged species in a solution to the surface of a working electrode,[23-30] the effect of various nucleation morphologies on photoelectrochemical deposition and *in-situ* synthesis of semiconductors onto non-photoactive substrates[35-39] is not well-elucidated or understood mechanistically at present. The long-range order of phototropically grown Se-Te films, as measured using Fourier-transform analysis, varies for growths on different substrates.[40] We observed previously through 2D Fourier-transform (2D FT) analysis that, under nominally identical illumination conditions, the lamellar pattern fidelity was higher when Se-Te films were deposited on crystalline (111)-oriented Si degenerately doped with p-type dopants (p^+-Si) than with n-type dopants (n^+-Si). A more highly ordered lamellar morphology was also observed on p^+-Si under conditions that resulted in dark and light current densities nominally identical to those measured on n^+-Si. We attributed the variations in pattern fidelity to effects of the type of junction formed between the substrate and the growing Se-Te film. Consistently, higher fidelity patterns were observed on substrates forming ohmic contacts to Se-Te (i.e. p^+-Si and Au) whereas patterns on substrates forming non-ohmic contacts to Se-Te (i.e. n^+-Si and Ti) consistently exhibited defects and lower pattern fidelity. The data herein confirm the hypothesis that the electrical contact differences between Se-Te films and n-Si or p-Si substrates primarily serve to produce different levels of disorder in the dark growth phase of the material, and the resulting differences in disorder between the dark electroplated films inherently and inevitably produce different amounts of spatial order in the resulting phototropically grown Se-Te overlayers.

The interaction of light with semiconducting electrodes can produce films with three-dimensional morphologies that are not accessible through other materials-processing techniques. For example, illumination of p-Si microwires during the electrodeposition of metals results in rings of metal nanoparticles at positions that are determined by the wavelength of illumination,[41] and illumination of Cu_2O microcrystals during electrochemical etching results in facet-selective deposition of metallic Cu shells.[42] Moreover, depending on the work function of the metal, illuminating macroporous p-type silicon during metal electrodeposition can spatially direct mass to deposit in patterns that are not accessible by dark depositions.[43]

Other structures have been fabricated with periodic morphologies determined by the wavelength and direction of polarization of incident light. For example, sub-micron scale periodic structures have been observed to form in azo-dye polymer films when illuminated with light near the dye's absorption band due to the *cis-trans* isomerization and subsequent structural reorientation of azo-dye molecules inside the polymer film.[44] Another phenomenon, laser-induced periodic surface structures (LIPSS), has been used to produce sub-wavelength features as small as $\lambda/10$.[45] Both of these phenomena have only been observed when using a coherent illumination source, i.e. a laser. In addition, LIPSS requires high-power illumination near the ablation threshold of the material being patterned, often in the kW cm^{-2} or MW cm^{-2} range. In contrast, phototropic growth of Se-Te lamellae has no requirement for illumination coherency and can be performed under illumination intensities of < 10 mW cm^{-2}.

Phototropically grown films adopt morphologies similar to the lamellar structures observed in biological systems (e.g. butterfly wings) in which they often demonstrate structural coloration and anisotropic de-wetting useful for self-cleaning.[46-48] As a proof of concept, materials engineered via LIPSS with similar morphologies to butterfly wings have demonstrated both structural coloration and especially large (>150°) contact angles for water.[49-50] As a bottom-up, solution-based fabrication method, phototropic growth presents an inexpensive, scalable, and highly tunable alternative to fabrication of these biomimetic structures. Improvements in the long-range order of phototropically grown films will result in increased levels of lamellar anisotropy and will likely improve the usefulness of the patterned structures in various applications, including self-cleaning surfaces and structural coloration elements.

CONCLUSION.

In inorganic phototropic growth, an initially isotropic dark nucleation spontaneously yields anisotropic spatially ordered nanostructures. Though principally an optically driven process, the phototropic growth model predicts that random variation in the dark electrodeposition process produces sites of surface roughness that scatter incoming illumination. As the deposition progresses, a subset of the initially random distribution of nucleates is selected where absorption "hot-spots" occur due to scattered light from nearby sites. These optically selected sites exhibit increased rates of mass addition due to the surface photovoltaic effect, leading to the observation and persistence of lamellar nanostructures. The distribution of Se-Te nucleates during the early stages of photoelectrodeposition depends on the applied deposition potential and substrate. Due to electrical junction effects,[40] Se-Te deposition on p^+-Si substrates produces smaller nucleate spacings than on n^+-Si substrates. However, nucleate spacings on n^+-Si were decreased considerably, and the resulting Se-Te pattern fidelities improved, by adjusting the applied deposition potential during an initial potential-striking step. In general, pattern fidelities were high when nucleate spacings were small. Small nucleation spacings also resulted in phototropic Se-Te films with lamellar patterns with periods that strongly agreed with a predicted trend of $\lambda/2n$.

Perhaps enigmatically, our results show that higher pattern fidelity and longer-range order in phototropically grown Se-Te films requires initial conditions of more disorder, or randomness, in the initial dispersion of scattering sites (nucleates). Contrary to previous phototropic growth studies (Table S1), this study demonstrates that the early distribution of nucleates is fundamental in determining pattern fidelity in phototropic films. For instance, phototropic growth of Se-Te films on Au substrates follows the observed trend of increased pattern fidelity at smaller nucleate spacings (Figure S14-15). Given that the photo-driven mass deposition can only occur where light is absorbed, a more uniform nucleation layer allows the developing film to adopt a morphology that is primarily influenced by local light absorption, maximizing the contribution from the self-optimized scattering and absorption feedback mechanism. Conversely, a less uniform nucleation layer with larger spacings between nucleates results in a growth process in which the pattern fidelity is the result of the convolution of the local field intensity and a non-uniform layer of mass. Thus, the distribution of the first nucleated particles deposited can strongly influence the resulting pattern fidelity in phototropic Se-Te films after ~200 times more mass has been deposited than in the initial dark nucleation process.

ELECTRONIC SUPPLEMENTARY INFORMATION.

In-depth experimental methods and materials used, additional scanning electron micrographs, discussion of pattern fidelity and peak-fitting procedures in 2D FT spectra, high-resolution FT spectra, mechanistic schemes.

AUTHOR INFORMATION.

Corresponding Author

*Email: nslewis@caltech.edu.

Notes

The authors declare no competing financial interest.

ACKNOWLEDGEMENTS.

This work was supported by the National Science Foundation under Award Number DMR1905963. The authors acknowledge Kathryn Hamann for assistance with image collection. L.X.V.M. acknowledges financial support from the Richard H. Cox SURF Fellowship.

REFERENCES.

1. Ito, T.; Okazaki, S., Pushing the limits of lithography. *Nature* **2000,** *406* (6799), 1027-31.
2. Martinsson, H., Current status of optical maskless lithography. *Journal of Micro/Nanolithography, MEMS, and MOEMS* **2005,** *4* (1), 011003.
3. Van den Hove, L.; Wong, A. K. K.; Ferguson, R. A.; Liebmann, L. W.; Mansfield, S. M.; Molless, A. F.; Neisser, M. O., Lithographic effects of mask critical dimension error. **1998,** *3334*, 106.
4. Postnikov, S.; Hector, S.; Garza, C.; Peters, R.; Ivin, V., Critical dimension control in optical lithography. *Microelectronic Engineering* **2003,** *69* (2-4), 452-458.
5. Groves, T. R., Statistics of pattern placement errors in lithography. *Journal of Vacuum Science & Technology B: Microelectronics and Nanometer Structures* **1991,** *9* (6), 3555.
6. Soh, H. T.; Guarini, K. W.; Quate, C. F., Introduction to Scanning Probe Lithography. **2001,** *7*, 1-22.
7. Wang, Z.; Tan, J.; Zou, Q.; Jiang, W., Mechanical-plowing-based high-speed patterning on hard material via advanced-control and ultrasonic probe vibration. *Rev Sci Instrum* **2013,** *84* (11), 113704.
8. Gordon, C. G., Generic criteria for vibration-sensitive equipment. *Proc. SPIE* **1992,** *1619*, 71-85.
9. Khoo, I.-C.; Chigrinov, V. G.; Kwok, H.; Yip, W. C.; Kozenkov, V. M.; Prudnikova, E. K.; Tang, B. Z.; Salhi, F., New photo-aligning and photo-patterning technology: superthin internal polarizers, retarders, and aligning layers. *Proc. SPIE* **2001,** *4463*, 117.
10. Song, X.; Fu, D.; Shah, S.; Reif, J., UV-Micropatterned Miniaturization: Rapid In Situ Photopatterning and Miniaturization of Microscale Features on Shrinkable Thermoplastics. *Advanced Materials Technologies* **2020**, 2000146.
11. Schmuki, P.; Erickson, L. E., Selective high-resolution electrodeposition on semiconductor defect patterns. *Phys Rev Lett* **2000,** *85* (14), 2985-8.
12. Bera, D.; Kuiry, S. C.; Seal, S., Synthesis of nanostructured materials using template-assisted electrodeposition. *Jom* **2004,** *56* (1), 49-53.
13. Liu, J.; Wernette, D. P.; Lu, Y., Proofreading and error removal in a nanomaterial assembly. *Angew Chem Int Ed Engl* **2005,** *44* (44), 7290-3.
14. Carim, A. I.; Hamann, K. R.; Batara, N. A.; Thompson, J. R.; Atwater, H. A.; Lewis, N. S., Template-free synthesis of periodic three-dimensional PbSe nanostructures via photoelectrodeposition. *J Am Chem Soc* **2018,** *140* (21), 6536-6539.
15. Carim, A. I.; Batara, N. A.; Premkumar, A.; Atwater, H. A.; Lewis, N. S., Self-Optimizing Photoelectrochemical Growth of Nanopatterned Se-Te Films in Response to the Spectral Distribution of Incident Illumination. *Nano Lett* **2015,** *15* (10), 7071-6.
16. Carim, A. I.; Batara, N. A.; Premkumar, A.; Atwater, H. A.; Lewis, N. S., Polarization Control of Morphological Pattern Orientation During Light-Mediated Synthesis of Nanostructured Se-Te Films. *ACS Nano* **2016,** *10* (1), 102-11.
17. Sadtler, B.; Burgos, S. P.; Batara, N. A.; Beardslee, J. A.; Atwater, H. A.; Lewis, N. S., Phototropic growth control of nanoscale pattern formation in photoelectrodeposited Se-Te films. *Proc Natl Acad Sci U S A* **2013,** *110* (49), 19707-12.
18. Carim, A. I.; Batara, N. A.; Premkumar, A.; May, R.; Atwater, H. A.; Lewis, N. S., Morphological Expression of the Coherence and Relative Phase of Optical Inputs to the Photoelectrodeposition of Nanopatterned Se-Te Films. *Nano Lett* **2016,** *16* (5), 2963-8.

19. Majidi, H.; Van, K. T.; Baxter, J. B., Nucleation and Growth of Extremely Thin CdSe Films Electrodeposited from Near-Neutral Electrolytes. *Journal of The Electrochemical Society* **2012,** *159* (10), D605-D610.
20. Hamann, K. R.; Carim, A. I.; Meier, M. C.; Thompson, J. R.; Batara, N. A.; Yermolenko, I. S.; Atwater, H. A.; Lewis, N. S., Optically tunable mesoscale CdSe morphologies via inorganic phototropic growth. *Journal of Materials Chemistry C* **2020**.
21. Yi, S.; Zhu, Z.; Cai, X.; Jia, Y.; Cho, J. H., The Nature of Bonding in Bulk Tellurium Composed of One-Dimensional Helical Chains. *Inorg Chem* **2018,** *57* (9), 5083-5088.
22. Springborg, M.; Jones, R. O., Sulfur and selenium helices: Structure and electronic properties. *The Journal of Chemical Physics* **1988,** *88* (4), 2652-2658.
23. Scharifker, B.; Hills, G., Theoretical and experimental studies of multiple nucleation. *Electrochimica Acta* **1983,** *28* (7), 879-889.
24. Morin, S.; Lachenwitzer, A.; Magnussen, O. M.; Behm, R. J., Potential-Controlled Step Flow to 3D Step Decoration Transition: Ni Electrodeposition on Ag(111). *Physical Review Letters* **1999,** *83* (24), 5066-5069.
25. Oskam, G.; Long, J. G.; Natarajan, A.; Searson, P. C., Electrochemical deposition of metals onto silicon. *Journal of Physics D: Applied Physics* **1998,** *31* (16), 1927-1949.
26. Paunovic, M., Electrochemical Deposition. In *Encyclopedia of Electrochemistry*, Bard, A. J.; Stratmann, M., Eds. Wiley-VCH Verlag GmbH & Co. KGaA: Weinheim, 2007.
27. Radisic, A.; Vereecken, P. M.; Searson, P. C.; Ross, F. M., The morphology and nucleation kinetics of copper islands during electrodeposition. *Surface Science* **2006,** *600* (9), 1817-1826.
28. Guo, L.; Searson, P. C., On the influence of the nucleation overpotential on island growth in electrodeposition. *Electrochimica Acta* **2010,** *55* (13), 4086-4091.
29. Palomar-Pardavé, M.; Scharifker, B. R.; Arce, E. M.; Romero-Romo, M., Nucleation and diffusion-controlled growth of electroactive centers. *Electrochimica Acta* **2005,** *50* (24), 4736-4745.
30. Krumm, R.; Guel, B.; Schmitz, C.; Staikov, G., Nucleation and growth in electrodeposition of metals on n-Si(111). *Electrochimica Acta* **2000,** *45* (20), 3255-3262.
31. Sharma, A. K., Electrodeposition of gold on magnesium-lithium alloys. *Metal Finishing* **1988,** *86* (12), 33-34.
32. Bewick, A.; Fleischmann, M.; Thirsk, H. R., Kinetics of the electrocrystallization of thin films of calomel. *Transactions of the Faraday Society* **1962,** *58*, 2200.
33. Ivanova, Y. A.; Ivanou, D. K.; Streltsov, E. A., Electrochemical deposition of PbTe onto n-Si(100) wafers. *Electrochemistry Communications* **2007,** *9* (4), 599-604.
34. Bijani, S.; Schrebler, R.; Dalchiele, E. A.; Gabas, M.; Martinez, L.; Ramos-Barrado, J. R., Study of the Nucleation and Growth Mechanisms in the Electrodeposition of Micro- and Nanostructured Cu2O Thin Films. *J Phys Chem C* **2011,** *115* (43), 21373-21382.
35. Phillips, R. J.; Shane, M. J.; Switzer, J. A., Electrochemical and photoelectrochemical deposition of thallium(III) oxide thin films. *Journal of Materials Research* **2011,** *4* (4), 923-929.
36. Tan, C.; Qin, C.; Sadtler, B., Light-directed growth of metal and semiconductor nanostructures. *Journal of Materials Chemistry C* **2017,** *5* (23), 5628-5642.
37. Lowe, James M.; Yan, Q.; Benamara, M.; Coridan, R. H., Direct photolithographic patterning of cuprous oxide thin films via photoelectrodeposition. *J. Mater. Chem. A* **2017,** *5* (41), 21765-21772.

38. Lancaster, M.; Mow, R.; Liu, J.; Cheek, Q.; MacInnes, M. M.; Al-Jassim, M. M.; Deutsch, T. G.; Young, J. L.; Maldonado, S., Protection of GaInP2 Photocathodes by Direct Photoelectrodeposition of MoSx Thin Films. *ACS Appl Mater Interfaces* **2019,** *11* (28), 25115-25122.
39. Windheim, J. v.; Darkowski, A.; Cocivera, M., Photoelectrochemical deposition and properties of thin-film cadmium telluride. *Canadian Journal of Physics* **1987,** *65* (8), 1053-1059.
40. Simonoff, E.; Lichterman, M. F.; Papadantonakis, K. M.; Lewis, N. S., Influence of Substrates on the Long-Range Order of Photoelectrodeposited Se-Te Nanostructures. *Nano Lett* **2019,** *19* (2), 1295-1300.
41. Dasog, M.; Carim, A. I.; Yalamanchili, S.; Atwater, H. A.; Lewis, N. S., Profiling Photoinduced Carrier Generation in Semiconductor Microwire Arrays via Photoelectrochemical Metal Deposition. *Nano Lett* **2016,** *16* (8), 5015-21.
42. Qin, C.; Campbell, B. M.; Shen, M.; Zhao, T.; Sadtler, B., Light-Driven, Facet-Selective Transformation of Cuprous Oxide Microcrystals to Hollow Copper Nanoshells. *Chemistry of Materials* **2019,** *31* (19), 8000-8011.
43. Ogata, Y.; Kobayashi, K.; Motoyama, M., Electrochemical metal deposition on silicon. *Current Opinion in Solid State and Materials Science* **2006,** *10* (3-4), 163-172.
44. Hubert, C.; Fiorini-Debuisschert, C.; Maurin, I.; Nunzi, J. M.; Raimond, P., Spontaneous Patterning of Hexagonal Structures in an Azo-Polymer Using Light-Controlled Mass Transport. *Advanced Materials* **2002,** *14* (10), 729.
45. Bonse, J.; Krüger, J.; Höhm, S.; Rosenfeld, A., Femtosecond laser-induced periodic surface structures. *Journal of Laser Applications* **2012,** *24* (4), 042006.
46. Chen, G.; Cong, Q.; Feng, Y.; Ren, L., Study on the wettability and self-cleaning of butterfly wing surfaces. In *Design and Nature II*, Collins, M. W.; Brebbia, C. A., Eds. WIT Press: Southampton (United Kingdom) and Billerica (Massachusetts), 2004; pp 245-251.
47. Sun, G.; Fang, Y.; Cong, Q.; Ren, L.-q., Anisotropism of the Non-Smooth Surface of Butterfly Wing. *Journal of Bionic Engineering* **2009,** *6* (1), 71-76.
48. Kinoshita, S.; Yoshioka, S.; Fujii, Y.; Okamoto, N., Photophysics of structural color in the Morpho butterflies. *Forma* **2002,** *17*, 103-121.
49. Martínez-Calderon, M.; Rodríguez, A.; Dias-Ponte, A.; Morant-Miñana, M. C.; Gómez-Aranzadi, M.; Olaizola, S. M., Femtosecond laser fabrication of highly hydrophobic stainless steel surface with hierarchical structures fabricated by combining ordered microstructures and LIPSS. *Applied Surface Science* **2016,** *374*, 81-89.
50. Long, J.; Fan, P.; Zhong, M.; Zhang, H.; Xie, Y.; Lin, C., Superhydrophobic and colorful copper surfaces fabricated by picosecond laser induced periodic nanostructures. *Applied Surface Science* **2014,** *311*, 461-467.

FIGURES.

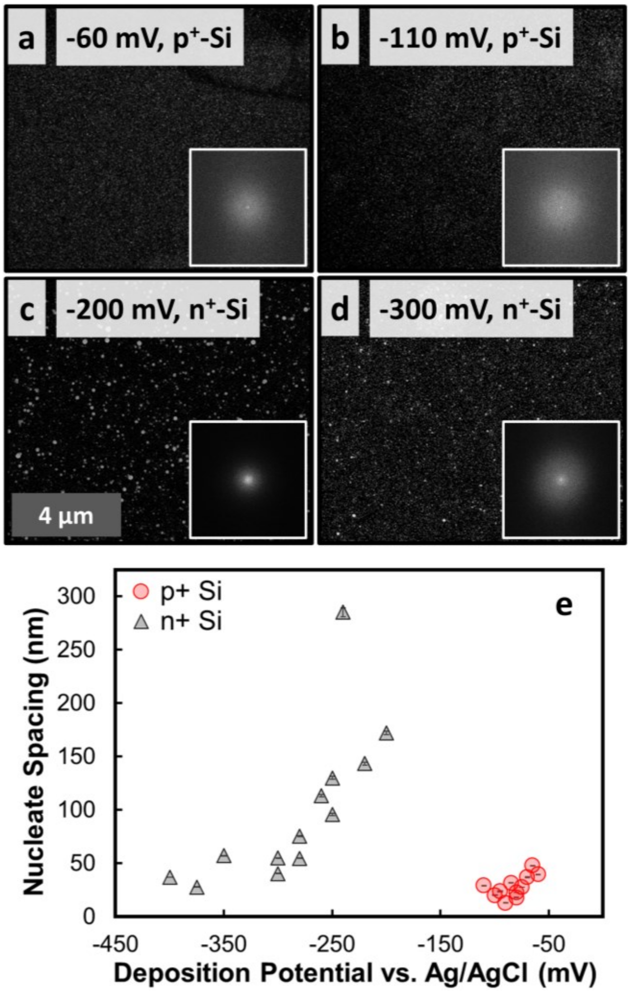

Figure 1. SEM images of Se-Te photoelectrodeposited at two different applied potentials on (a, b) p^+-Si and (c, d) n^+-Si. During the deposition, the substrates were illuminated by vertically polarized light from a narrow-band LED with $\lambda = 927$ nm at a power density of 53 mW cm^{-2}. For each image, the charge density passed was -3.75 mC cm^{-2}. The deposition potentials are referenced to Ag/AgCl. Insets to (a)-(d) are 2D FT of large-area images of the respective films, scale of inset side is 85.6 μm^{-1}. (e) Dependence of average particle-to-particle spacing on deposition potential for various Se-Te films deposited on p^+-Si and n^+-Si substrates after passing a charge density of -3.75 mC cm^{-2}.

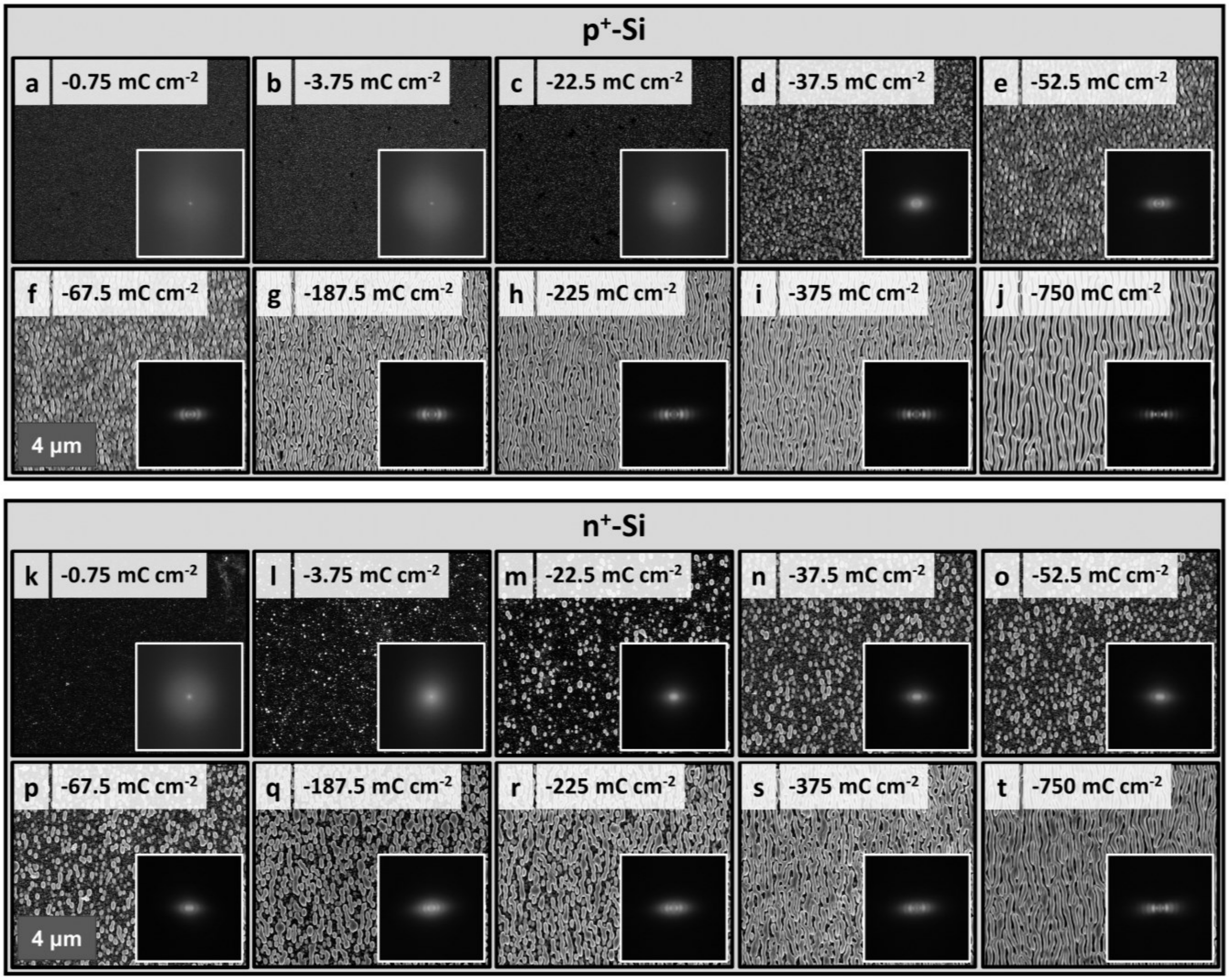

Figure 2. Series of SEM images demonstrating representative morphology of films deposited on (a)-(j) p^+-Si at -80 mV vs. Ag/AgCl and (k)-(t) n^+-Si at -250 mV vs. Ag/AgCl with characteristic amounts of charge passed (mass deposited) per unit area of: (a), (k) -0.75 mC cm^{-2}; (b), (l) -3.75 mC cm^{-2}; (c), (m) -22.5 mC cm^{-2}; (d), (n) -37.5 mC cm^{-2}; (e), (o) -52.5 mC cm^{-2}; (f), (p) -67.5 mC cm^{-2}; (g), (q) -187.5 mC cm^{-2}; (h), (r) -225 mC cm^{-2}; (i), (s) -375 mC cm^{-2}; and (j), (t) -750 mC cm^{-2}. Insets to (a)-(t) are 2D FT of large-area images of the respective films, scale of inset side is 85.6 μm^{-1}.

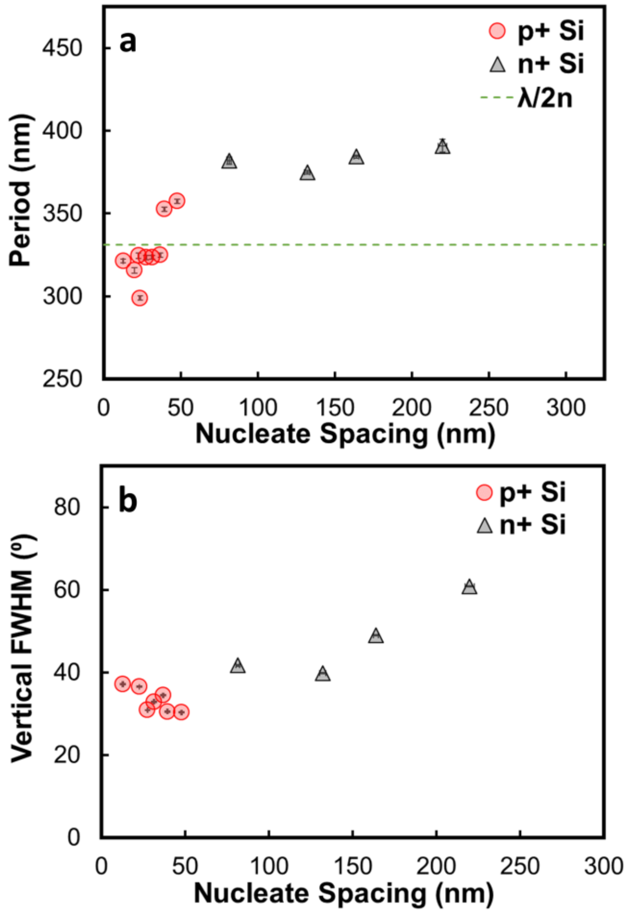

Figure 3. Relationship between the average particle-to-particle spacing of nucleated films at early levels of mass deposition (-3.75 mC cm^{-2}) and (a) the observed lamellar period and (b) pattern fidelity as described by the vertical (parallel to axis of polarization) FWHM of the primary peak in the 2D FT of imaged Se-Te films. The lamellar period predicated by an optical model and observed in prior results is $\lambda/2n$ and is indicated in (a). The variation in nucleate spacing for deposits on either p$^+$-Si or n$^+$-Si substrates was due to a difference in applied deposition potential, as shown in Figure 1. The films that were analyzed to obtain lamellar period and vertical FWHM values were deposited at a charge density of -750 mC cm^{-2}. Vertical FWHM and pattern period values are paired with corresponding particle spacing values that share applied deposition potentials ranging from -60 to -100 mV vs. Ag/AgCl for p$^+$-Si and -200 to -300 mV vs. Ag/AgCl for n$^+$-Si.

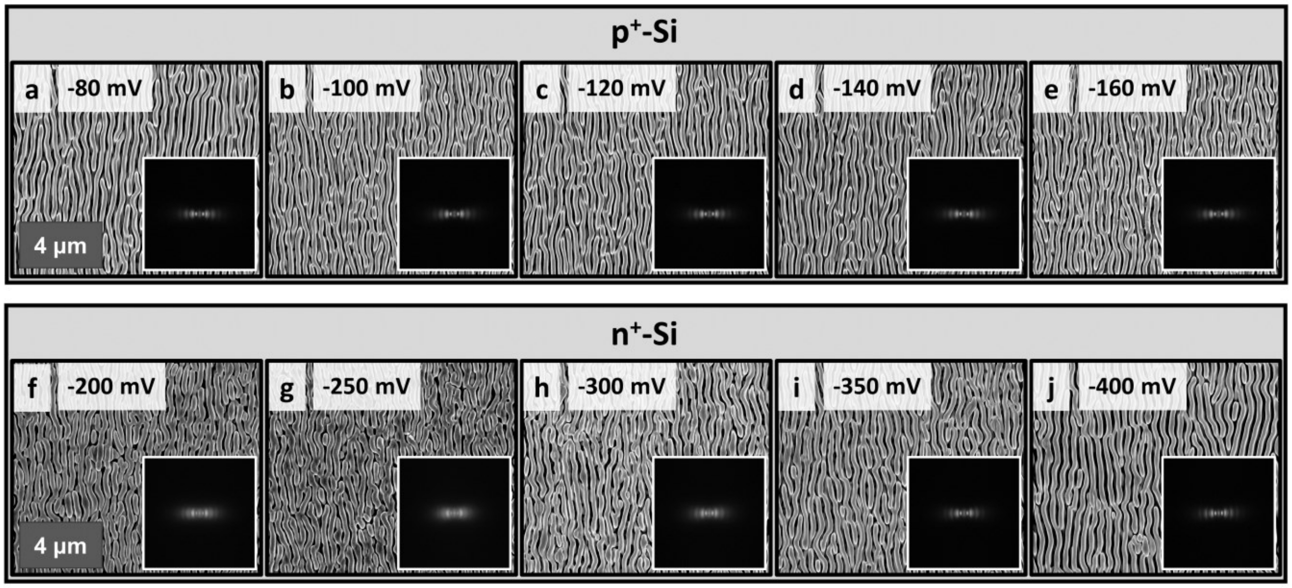

Figure 4. Series of SEM images demonstrating representative morphology of films deposited to a total of -750 mC cm^{-2} on (a)-(e) p^{+}-Si at -80 mV vs. Ag/AgCl and (f)-(j) n^{+}-Si at -200 mV vs. Ag/AgCl after depositing -3.75 mC cm^{-2} in an applied potential strike step. (a) control at -80 mV and striking potentials of (b) -100 mV, (c) -120 mV, (d) -140 mV, and (e) -160 mV vs. Ag/AgCl on p^{+}-Si. (f) control at -200 mV and striking potentials of (g) -250 mV, (h) -300 mV, (i) -350 mV, and (j) -400 mV vs. Ag/AgCl on n^{+}-Si. Insets to (a)-(t) are 2D FT of large-area images of the respective films, scale of inset side is 85.6 μm^{-1}.

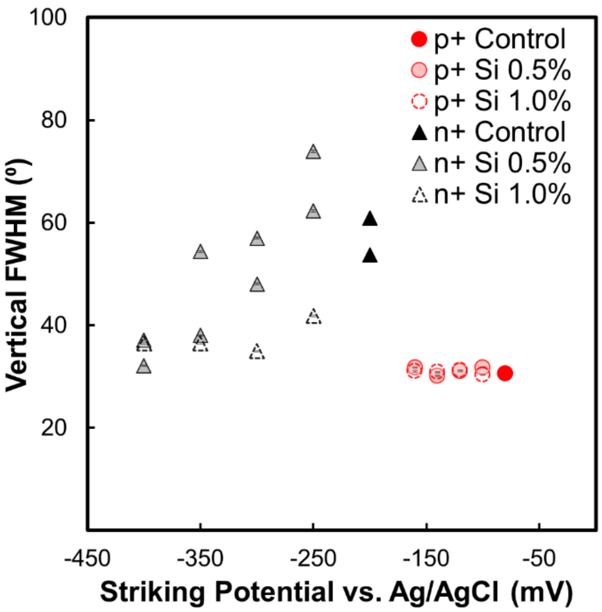

Figure 5. Relationship between striking potential and pattern fidelity as described by the vertical (parallel to axis of polarization) FWHM of the primary peak in the 2D FT of imaged Se-Te films. The striking-potential step was performed on p^+-Si and n^+-Si substrates until a charge density of either -3.75 mC cm^{-2} (0.5%) or -7.5 mC cm^{-2} (1.0%) had been passed. The remainder of the charge density (to -750 mC cm^{-2}) was passed at -80 mV (p^+-Si) and -200 mV (n^+-Si) vs. Ag/AgCl. Control experiments are Se-Te films deposited without any striking-potential step.